annalen der physik
www.ann-phys.org

An Infrared Metamaterial Broadband Absorber Based on a Simple Titanium Disk with High Absorption and a Tunable Spectral Absorption Band

Yinhui Tang, Dejia Meng, Zhongzhu Liang, Zheng Qin, Xiaoyan Shi, Yuhao Zhang, Ying Xiong, Yandong Fan, Fuming Yang, Lichao Zhang, Jingguang Lv, Yuxin Qin, Changhong Chen, and Jianjun Lai*

A metamaterial absorber is proposed that functions in the medium- (3–5 μm) and long-wavelength (8–12 μm) infrared (medium-wavelength infrared, MWIR, and long-wavelength infrared, LWIR, respectively) regions. The proposed design, which consists of periodic cells, can be tuned to achieve single-band or dual-band light absorption by changing the periodicity of the structure. Each cell forming the metamaterial absorber consists of a bottom metal plate (Al), a top metal disk (Ti), and an intermediate dielectric medium (Si or ZnS) in which a metal disk (Ti) is embedded. For a period of 0.85 μm, the absorber achieves broadband absorption in the LWIR region, with an average absorption of 92.1%. Further, the absorber shows acceptable tolerance to irradiation at oblique incidence. For a period of 2 μm, a peak absorption of 99.05% is achieved in the MWIR region, thereby providing dual-band absorption. Tuning the periodicity of the structure enhances the localized surface plasmon resonance, with the absorption mechanism explained by establishing an equivalent parallel LC circuit. The absorption properties demonstrated by the proposed metamaterial absorber are promising for thermal imaging and infrared spectroscopy.

1. Introduction

Electromagnetic wave absorbers have been a hot topic in scientific research for decades,[1–4] with materials approximating black body behavior of particular interest to engineers. Metamaterials are artificial materials for which the dielectric constant is controlled, through structural design and material selection, to deliver tailored optical or acoustic properties; the blackbody absorption of light for specific wavelength ranges is one such property that can be realized using metamaterials. Metamaterial absorbers have found application in diverse fields, including biosensing, solar power, thermal imaging, infrared spectroscopy, and optical gas sensing.[5-10]

The first microwave metamaterial absorbers were demonstrated experimentally by Landy et al.,[11] since when there have been many reports describing terahertz, infrared, and visible metamaterial absorbers.[12-15] Metamaterial absorbers function via the principle that plasmon resonances produced by light incident on a metal surface significantly enhance the electromagnetic field around the metal medium.[16] Plasmon resonance is a coupled surface electromagnetic mode formed by free electrons on a metal surface interacting with photons under the excitation of a light field. It is usually categorized as either propagating surface plasmon resonance (PSPR) or local surface plasmon resonance (LSPR). Absorption is due to polarized waves generated by electronic oscillations causing metal and dielectric losses.[17,18] For infrared detection, it is often necessary to capture infrared signals in the atmospheric window (i.e., 3–5 and 8–14 μm).[19,20] Compared with traditional microcavity absorption, metamaterials can achieve higher absorption with thinner material thicknesses.[21] Previous studies have explored the use of metal resonator structure metamaterials (including both 2D and 3D designs) to achieve perfect absorption within specific wavelength bands.[22-24] Although these structures yielded strong absorption effects, the large size and narrow bandwidth of the absorption limit its development. Several methods for increasing

Dr. Y. Tang, Dr. D. Meng, Prof. Z. Liang, Dr. Z. Qin, Dr. X. Shi, Dr. Y. Zhang, Dr. Y. Xiong, Dr. Y. Fan, Dr. F. Yang, Dr. L. Zhang, Dr. J. Lv, Dr. Y. Qin
State Key Laboratory of Applied Optics
Changchun Institute of Optics
Fine Mechanics and Physics
Chinese Academy of Sciences
Changchun, Jilin 130033, China
E-mail: liangzz@ciomp.ac.cn

Dr. Y. Tang, Dr. Z. Qin, Dr. X. Shi, Dr. Y. Zhang, Dr. Y. Xiong, Dr. Y. Fan, Dr. F. Yang
University of the Chinese Academy of Sciences
Beijing 100049, China

Prof. C. Chen, Prof. J. Lai
Wuhan National Laboratory for Optoelectronics
Huazhong University of Science and Technology
Wuhan 430074, China

The ORCID identification number(s) for the author(s) of this article can be found under https://doi.org/10.1002/andp.202000145

DOI: 10.1002/andp.202000145

the absorption bandwidth have been reported, such as increasing the number of metal dielectric layers, or performing complex patterning on the top metal to stimulate different resonance modes.[25-28] The disadvantage of these methods is that the thickness of the absorber is increased, while the manufacturing process is both difficult and expensive. Therefore, it is necessary to develop and design an effective broadband absorber that has a simple structure, is easy to manufacture, and corresponds to the infrared window. In addition, multispectral detection has been shown to improve detection accuracy and reduce noise; it can distinguish detected objects from the background based on the characteristics of the target.[29,30] Therefore, multispectral detection is a further desirable property for new absorber designs. In general, dual-band absorbers are relatively large and are often composed of absorber units with different characteristic sizes, which adds to the complexity of the manufacturing process and decreases the duty ratio of absorber cells.[31,32]

Here, we propose an infrared metamaterial absorber structure. The structure operates within the atmospheric window, and thus provides optimal functionality in the infrared band. Our design is a single structure with small size and easy to manufacture. The absorber has a simple structure with a high absorption performance, and it can be applied to broadband LWIR absorption and multispectral infrared detection. For a period of 0.85 μm, the proposed absorber exhibits absorption within the 8–12 μm wavelength range that reaches 91.5%. The absorption band is formed by the resonance coupling of two LSPRs. The influence of the incident angle on the absorption performance was tolerable, with the average absorption between 8 and 12 μm, reaching 83.75% and 88.5% for transverse magnetic (TM) (*E* perpendicular to the incident plane) and transverse electric (TE) (*H* perpendicular to the incident plane) waves, respectively, for an incident angle of 50°. By increasing the period, we excited the absorption peak based on the interaction of LSPR and PSPR between 3 and 5 μm, with the peak value approaching 100% and an 80% bandwidth of 0.66 μm. Therefore, the bandwidth of the proposed dual-band metamaterial absorber can be tuned by changing the period of the structure, and thus the absorber can realize tunable absorption in the medium wavelength infrared (MWIR) and long wavelength infrared (LWIR) spectral regions. For dual-band metamaterial absorber, the average absorption between 8 and 12 μm is >90%. By analyzing the electromagnetic field and establishing the LC model of the equivalent circuit, we explain the working mechanism of the proposed metamaterial absorber structure, thus revealing the reason for the excited absorption peak between 3 and 5 μm.

2. Design of LWIR Broadband Absorber

The absorber comprises a periodic array, as shown in **Figure 1**a. Each cell consists of a bottom metal plate, a top metal disk (Ti), and an intermediate medium embedded by a metal disk (Ti), as shown in Figure 1b. The length and width of the underlying metal and interlayer dielectric of each cell are *P*. The diameter and height of the top metal disk are w_1 and t_1, respectively. The diameter of the embedded metal disk is w_2, with height t_2. The distance from the lower surface of the embedded metal disk to the upper surface of the metal plate is *h*. The thickness

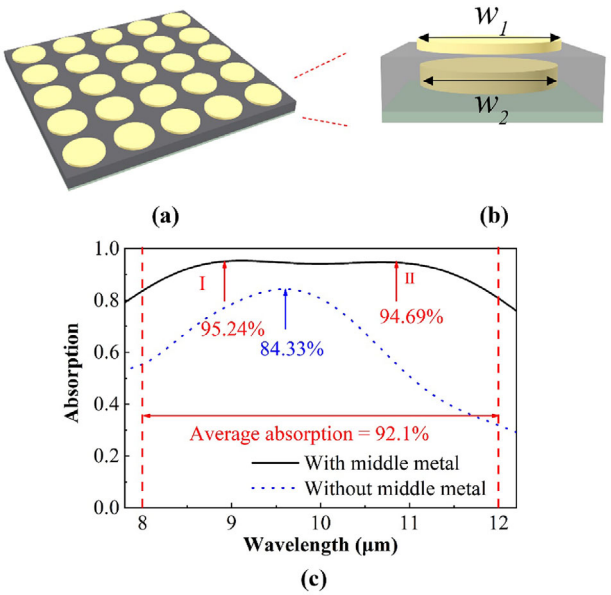

Figure 1. a) Schematic diagram of metamaterial absorber. b) Amplified structure of the absorber unit. c) The simulation calculation of absorption spectrum. The solid black line is the absorption spectrum of the absorber we designed, and the blue dotted line is the absorption spectrum of the traditional three-layer structure absorber.

of the bottom metal plate is 0.1 μm and the thickness of the intermediate medium is *m*.

2.1. Structural Parameters and Material Selection

Figure 1b shows the cell structure of the absorber with a period $P = 0.85$ μm. The bottom layer is an Al plate with a thickness of 0.1 μm. The intermediate layer is a Si dielectric layer with a thickness $m = 0.4$ μm. A Ti disk with a diameter $w_2 = 0.66$ μm and height $t_2 = 0.1$ μm is embedded in the dielectric layer. The distance between the lower surface of the embedded metal disk and the bottom metal plate is $h = 0.04$ μm. The top surface of the dielectric layer is bonded by a Ti disk (diameter $w_1 = 0.7$ μm and height 0.08 μm). The complex dielectric constants of Ti and Al were modeled using Drude–Lorentz fitting to tabulate the experimental data.[33,34] The dielectric constant of Si was calculated following a previous study.[35]

2.2. Results and Discussion

We used the finite-difference time-domain (FDTD) method to analyze the absorption spectrum of the absorber, as shown in Figure 1c. There is a wide absorption band with an average absorption of 92.1% between 8 and 12 μm. The absorption band is formed by the coupling of two relatively independent absorption peaks, with maximum absorption values of 95.24% (peak I at a wavelength of 9.00 μm) and 94.69% (peak II at 10.65 μm), respectively. To increase the average absorption, the two peaks are brought closer, but not excessively overlapping, by changing the structural parameter (embedded metal thickness). Compared with the traditional three-layer structure of an absorber (blue line in Figure 1c), our absorber design almost doubled the

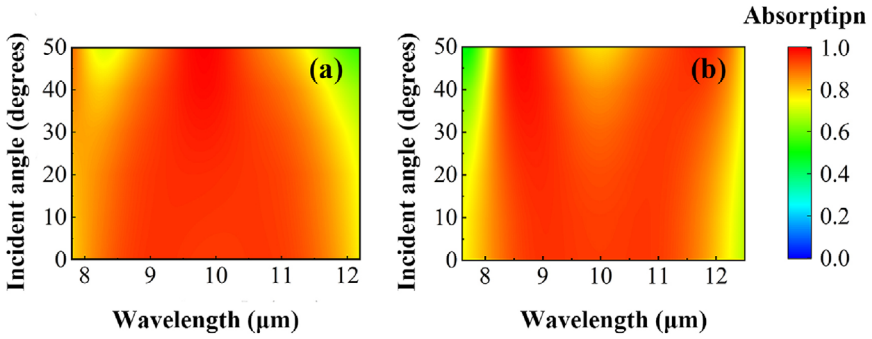

Figure 2. a,b) Absorption spectra with different incident angles for: a) TM–mode (*x*–polarized) and b) TE–mode (*y*–polarized).

absorption bandwidth, while also improving the absorption rate significantly.

We explored the influence of the incident angle on the performance of the absorber, as shown in **Figure 2**. The absorption performance showed high tolerance in response to the incident angle being increased. For TM waves (Figure 2a), as the incident angle increases, the interval between absorption peaks I and II decreases until they overlap, and the absorption rate at the center of the absorption band (10 μm) increases significantly. When the incident angle is increased to 50°, the absorption within the 8–12 μm reaches to 83.75%. In contrast, for the TE wave, absorption peaks I and II gradually tend to diverge, becoming more distinct from one another, as shown in Figure 2b. When the incident angle is increased to 50°, the absorption reaches 88.5%, which is only 3.6% lower than at normal incidence. This shows that the absorption response is more resistant to changes in the angle under TE waves.

To analyze the origin of the two peaks, we observed the *X*–*Z* plane electromagnetic field distribution (**Figure 3**). Figure 3a,b shows the electromagnetic field distribution at peaks II (10.65 μm) and I (9.00 μm), respectively. For comparative purposes, Figure 3c shows the electromagnetic field distribution of the metal without an intermediate layer. Examining the electric field distributions, a clear magnetic field enhancement phenomenon can be seen near the metal, indicating that absorption peaks I and II are excited predominantly by LSPR. The light field energy is concentrated mainly in the dielectric medium between the intermediate layer metal and the lower surface metal. By observing the magnetic field distribution, the interlayer metal disk has a shielding effect on the magnetic field distribution. The difference of the incident light wavelength causes the difference of the magnetic field enhancement phenomenon area. The enhancement of the plasmon resonance magnetic field generating peak II occurs mainly in the medium between the embedded metal disk and the underlying metal plate. The enhancement of the plasmon resonance magnetic field generating the peak I occurs not only between the intermediate metal disk and the underlying metal plate, but also between the intermediate metal disk and the top metal disk, and is considered to be caused by two sets of resonances. Essentially, the wide absorption band is caused by the superposition of two sets of plasmon resonances.

The absorptive capacities of different parts of the structure are shown in **Figure 4**. Light absorption due to the dielectric layer is negligible; the overall absorption is composed predominantly

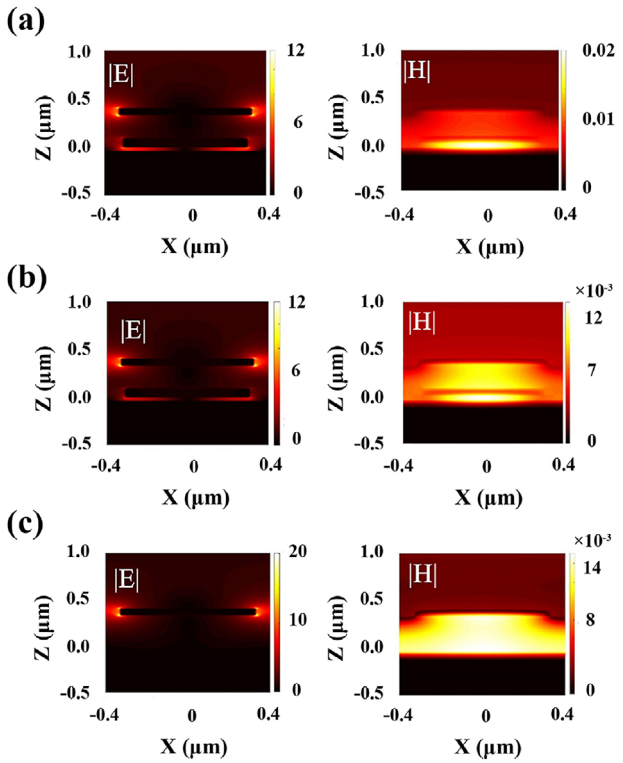

Figure 3. Distribution of electromagnetic fields at typical locations of the spectrum. a) Electromagnetic field distribution at 10.65μm for LWIR absorber. b) Electromagnetic field distribution at 9μm for LWIR absorber. c) Electromagnetic field distribution at the peak of absorption without a metal layer embedded in the middle.

of contributions from the two metal components, with the metal in the middle layer playing a leading role. This is different from a traditional three-layer absorber, for which the energy absorption is driven by the top metal disk or the bottom metal plate. For the proposed absorber design, the embedded absorber absorbs energy and concentrates it inside the wave absorber, which reduces the diffusion of energy to the environment and improves energy efficiency. The bottom metal plate has almost no absorption effect; its role is to reflect light only, thus preventing its transmittance. It can be concluded from the energy absorption distribution of different layers in Figure 4 that the absorption of the entire absorber structure occurs in the metal, with Ti playing an

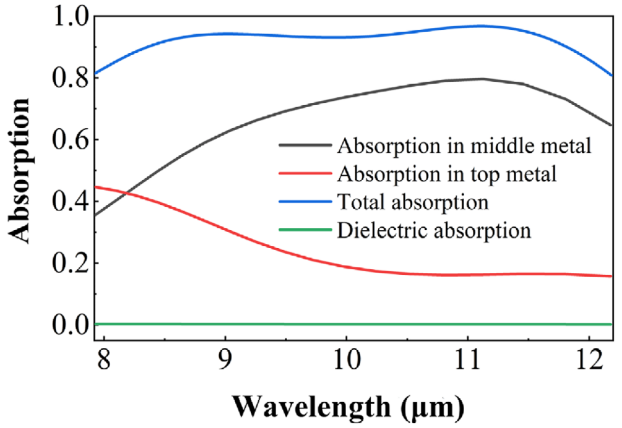

Figure 4. Absorption ability in different parts of the absorber.

important role in the entire absorption process. In addition, the absorption of the intermediate metal layer correlates is reflected in the magnetic field distribution, which corresponds to the magnetic field enhancement phenomenon between the intermediate metal layer and the bottom metal plate. This phenomenon also corresponds to peak II of the absorption spectrum. The absorption of the top metal, reflected in the magnetic field distribution, corresponds mainly to the enhancement of the magnetic field between the middle metal and the top metal. This field enhancement corresponds to peak I of the absorption curve. This result implies a correlation between the structure of the design, the distribution of the magnetic field, the absorption spectrum, and the absorption energy distribution.

To analyze the response of the absorber to light more completely and predict the effect of the structure and materials of the absorber on the absorption spectrum, we established an equivalent LC model to simulate the absorption of light by the absorber.[36,37] In the structure of the absorber, the embedded metal plays an electromagnetic shielding role. In the upper and lower areas of the embedded metal, the magnetic field increases, causing a ring current. Therefore, when implementing the equivalent LC model of the absorber, the equivalent resistances of the upper and lower magnetic field enhancement regions must be considered separately. The equivalent impedances of the upper and middle layers are connected in parallel with the equivalent impedance of the lower and middle layers to form a description of the absorber. **Figure 5**a is an equivalent circuit schematic diagram of the middle and upper layers of the metal and intermediate dielectric. C_{g1} represents the capacitance between the top metal and other cycles, and it is described by Equation (1). C_{g2} represents the capacitance between the interlayer metal and other cycles. The size of C_g is related to the permittivity and separation distance. C_{g1} can be described by Equation (1), where the top metal thickness is t_1. The distance from the other cells is proportional to P-w_1. The dielectric permittivity ϵ_0 represents the material between each cell of the metal (air in this case). C_m is the capacitance between the metals (top-middle or middle-bottom), which is related to the dielectric material and the thickness of the dielectric between the two metal disks. L is determined by the mutual inductance between the inductance caused by the drifting electrons and the metal. The equivalent circuits of the middle and

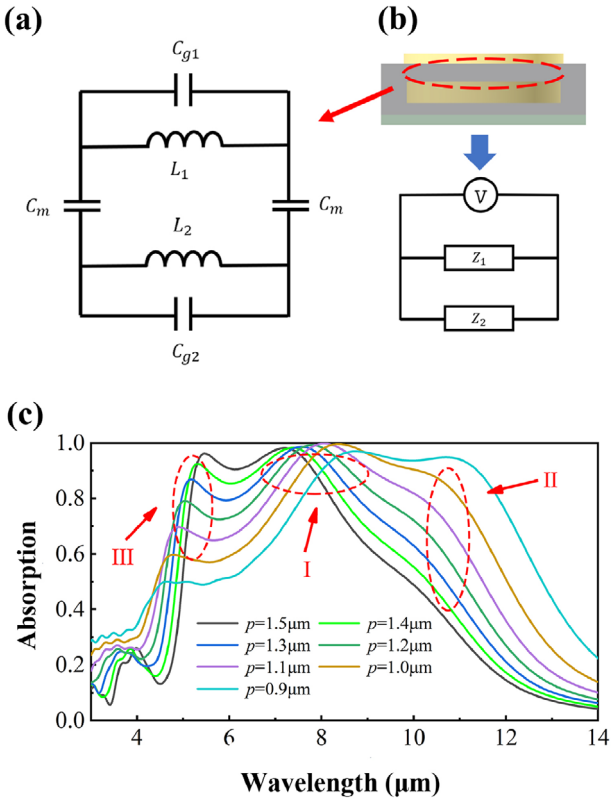

Figure 5. a) The equivalent circuit schematic diagram of the middle and upper layers of metal and intermediate dielectric. b) The absorber equivalent parallel circuit. c) Influence of period size (P) on absorption spectrum. The absorption spectra of different period are indicated by different color.

lower layers are similar to that shown in Figure 5a, except that there is no parallel connection of C_{g2}. The impedance of each part of Z_n is expressed by Equation (2). After calculating the upper-layer metal impedance Z_1 and the lower-layer metal impedance Z_2, a parallel circuit is formed to describe the absorber, as shown in Figure 5b. The total resistance is described by Equation (3). The changes in absorption can be mapped using changes in the total impedance

$$Z_n = \frac{2}{i\omega C_m} + \frac{i\omega L_1}{1-\omega^2 C_{g1} L_1} + \frac{i\omega L_2}{1-\omega^2 C_{g2} L_2} \quad (1)$$

$$C_{g1} = t_1 \epsilon_0 / (p - w_1) \quad (2)$$

$$\frac{1}{Z_{total}} = \frac{1}{Z_1} + \frac{1}{Z_2} \quad (3)$$

The absorption principle of the absorber can be understood as the resonance between light and polarized waves in the metal, which causes an increase in the intensity of the electromagnetic field. Irradiating the array induces an oscillating voltage. The array cell is equivalent to the LC circuit and the existence of the oscillating voltage will stimulate the generation of current in the circuit, which will cause the absorption of electromagnetic energy. The absorbed light energy is converted into thermal energy. It is

known that the equivalent current is inversely proportional to the impedance of the entire LC circuit, that is, when the impedance is 0, the current is the largest, and thus perfect absorption can be achieved. At wavelengths of 3–5 μm, as the period of the structure increases, the interval between the top metal disk of each cell becomes larger, which causes C_g to increase. The increase in C_g leads to the total impedance decreasing, as described by Equation (1). Based on the relationship between the current and impedance, an increase in impedance causes an increase in current. The increase in current results in an increase in absorption. By mathematical analysis of Equation 2, reducing the thickness of the top metal can also increase the capacitance, which results in an increase in absorption. By changing the period, the absorption peak can be excited in the 3–5 μm wavelength range, as shown in Figure 5c. As the period increases, a new absorption peak (peak III) is excited. By exciting these peaks, we design a dual-band tunable absorber.

3. Tunable Dual-Band Absorber

3.1. Structural Parameters and Material Selection

We increased the absorber period in the previous section to 2 μm, leading to the excitation of absorption peak III. The position of peak I in LWIR is blueshifted, while peak II was suppressed significantly, as shown in Figure 5c. To offset this peak suppression, we altered certain parameters of the absorber, including the position and thickness of the metal embedded in the dielectric medium and the size of the two metal disks. From the relationship between the absorption spectrum and structural parameters of the equivalent LC model, it was inferred that changing these parameters could achieve broadband absorption. In response to tailoring these structural parameters, peaks I and II in the LWIR were restored, demonstrating that the proposed structure can achieve broadband absorption in the LWIR region.

The choice of medium can affect the position of absorption peak III. ZnS, which has a smaller refractive index than Si, is investigated as an alternative dielectric medium.[38,39] Using ZnS as the dielectric material, the absorption peak at 5.5 μm is blueshifted to the mid-wave infrared band; however, the thickness of the absorber is increased. The structural parameters of the ZnS dual-band absorber are as follows: $P = 2$ μm, $w_2 = 1.5$ μm, $w_1 = 1.56$ μm, the thickness of the intermediate layer is 0.21 μm, the distance from the lower surface of the embedded metal to the underlying metal is $h = 0.06$ μm, and the thickness of the medium is $m = 0.5$ μm.

3.2. Result Analysis

The simulated absorbance behavior for the ZnS structure using the parameters listed above is shown in **Figure 6**. There is a 99.05% absorption peak at 4.59 μm with an 80% bandwidth of 0.66 μm, and the average absorption rate in the LWIR region of 8–12 μm reaches 90.5%. The average absorption in the region of 8–12 μm declines due to dielectric material changes. However, the absorption mechanism is the same as described in the previous section for the Si absorber.

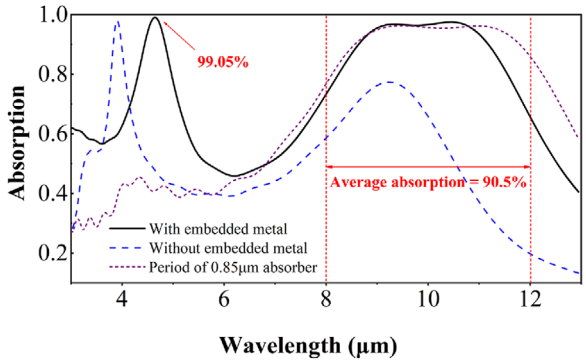

Figure 6. Absorption spectrum. The solid black line is the absorption spectrum of the dual-band absorber we designed. The blue dotted line is the absorption spectrum without embedded metal. The purple dotted line is the absorption spectrum of the broadband absorber with a small period 0.85μm mentioned in the previous chapter.

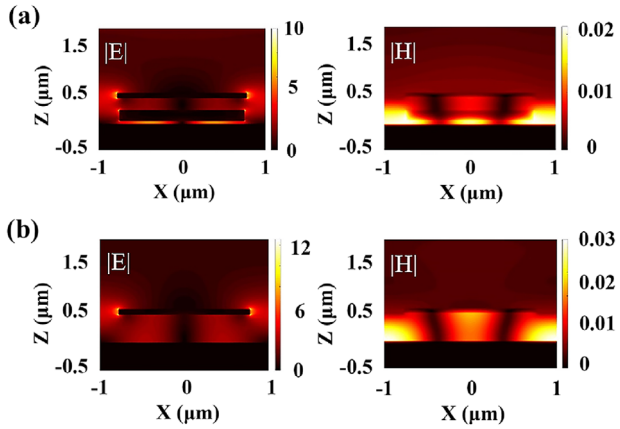

Figure 7. a) The electromagnetic field distribution at 4.59 μm (absorber with intermediate metal). b) The electromagnetic field distribution at 4 μm (absorber without intermediate metal).

In the previous section, increasing the period of the structure for the equivalent LC model resulted in the appearance of an additional absorption peak (peak III). To further analyze the origin of the peak in the mid-wave infrared region further, we observed the electromagnetic field distribution of the dual-band tunable absorber at the mid-wave absorption peak, as shown in **Figure 7**a. Regarding the electric field distribution, the electric field enhancement phenomenon occurred in both the upper layer and the intermediate metal. There is a magnetic field enhancement inside the middle layer and also a magnetic field enhancement on both sides of each cell. Therefore, we infer that the excitation peak III is mainly a combination of PSPR and LSPR. It can be observed from Figure 6 that there is a near-perfect absorption peak at 4.59 μm and that this strong absorption occurs in the 4–6 μm range irrespective of the cell size. The near-perfect absorption originates principally from the LSPR, which has a strong magnetic field enhancement phenomenon at 4.59 μm. The periodic edge magnetic field enhancement phenomenon, which is related to PSPR, not only occurs at 4.59 μm, but is also be observed in the 4–6 μm range of the electromagnetic field distribution. This suggests that PSPR has always contributed to absorption within

the 4–6 μm wavelength range, with the absorption manifested as a combination of different PSPR-enhanced peaks. Increasing the periodicity of the absorber structure has a significant effect on enhancing LSPR absorption. Observing the electromagnetic field distribution of a small-period absorber in the 3–5 μm wavelength range, we can see a strong PSPR phenomenon and a weak LSPR phenomenon, which confirms the above conclusion. The absorption due to PSPR complements that of LSPR, and thus achieves near perfect absorption. In the absence of an interlayer metal, the peaks in the region of LWIR and MWIR can also be obtained by excitation. The electromagnetic field distribution is shown in Figure 7b. Because there is no shielding effect of the intermediate metal, the energy distribution of the intermediate magnetic field is concentrated throughout the entire medium, and the absorption peak is blue-shifted. In addition, the lack of excitation peak in the LWIR region leads to a reduction in bandwidth and absorption. This is consistent with the property of the small-period structure.

3.3. Tuning Properties of Dual-Band Absorber

We studied the performance of the dual-band absorber in response to tuning specific parameters; namely, the diameter of the upper metal disk and the embedded metal disk only, with the other condition invariant. We demonstrated that the absorption band can be tuned in the LWIR region. We changed the size of w_1 and set $w_2 = w_1 - b$, where b changes with the size of w_1 and w_2. For convenience, an approximate constant b of 0.6 μm was used in the simulation. **Figure 8**a shows the relationship between absorption and wavelength with w_1 and w_2 change. As the parameter (w_1) increases, the entire absorption band moves toward the long wavelength. However, according to the analysis of the equivalent LC circuit model above (Figure 5), it can be seen that the gap between the metals affect the capacitance in the circuit, causing a subsequent decrease in the absorption peak; therefore, w_1 cannot be too large when tuning the absorption peak.

The analysis of the equivalent LC circuit model also demonstrated that changing the material of the dielectric layer changes the impedance in the equivalent circuit, effecting the position of the absorption peak. We investigated the behavior of the model using three different materials,[38-40] obtaining the result shown in Figure 8b. When the material of the dielectric layer is changed, the absorption peaks in both the MWIR and LWIR regions shift. However, it is possible to readjust the absorption peaks via tailoring the values of w_1 and w_2; this has a large effect in the LWIR region and less so for the MWIR region. By controlling the disk diameters and the dielectric material selection, independent regulation of the absorption peak can be accomplished. In addition, we replaced the underlying metal material and selected Al and Cu to prove that replacing the underlying material has little effect on the performance of the absorber. This is because the underlying metal of the structure designed in this study does not participate in the absorption mechanism and reflects light only.

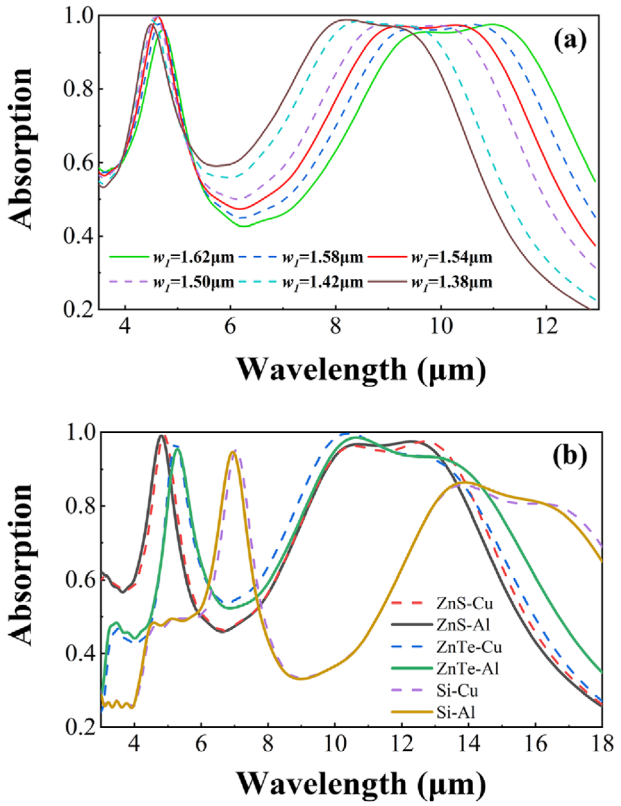

Figure 8. a) The absorption band of the long-wave infrared region is tunable. Changing the size of the middle and upper metal causes the position of the absorption band of the long-wave infrared region to change. Different color curves correspond to different top metal diameters(w_1). b) The effect of different medium materials on the absorption spectrum. The dielectric and bottom metal materials are changed. In the legend, the first half is the dielectric material used, and the second half is the bottom metal material.

4. Conclusion

In summary, we propose a simple metamaterial absorber design. The absorption peak of the absorber corresponds to the LWIR and MWIR atmospheric windows. The absorber is composed of a periodic cell that consists of a bottom metal plate (Al), a top metal disk (Ti), and an intermediate medium (Si or ZnS) in which a metal disk (Ti) is embedded. When the size of the absorber cell is 0.85 μm, it is possible to achieve broadband absorption by two LSPR absorption peaks in the 8–12 μm wavelength range. In this case, the average absorption by the structure was 92.1%. The absorption performance showed acceptable tolerance to changing the incident irradiation angle. For a 2 μm absorber cell is, using ZnS as the medium, not only is a wide band absorption with an average absorption of 90.5% achieved between 8 and 12 μm, but a 99.05% absorption peak is excited at 4.59 μm also. Our analysis of the absorption performance of the proposed design revealed that the upper and middle metals are the key components of the absorption mechanism. By establishing an equivalent LC model of the absorber, the reason for the absorption peak excitation can be explained as follows: owing to the increase in the period, the distance between the metal disks of different cells increases, causing the equivalent impedance in the LC circuit to increase, which in turn leads to an increase in current. The increased current enhances losses in the metals, leading to an increase in absorption. Based on the electromagnetic field distribution, we determined

that absorption enhancement is driven principally by LSPR and augmented by PSPR. Since the material and size parameters have different effects on the absorption of the absorber in different wavebands, the proposed design can realize a relatively independent shift tuning of the absorption peak. By changing the diameter of the metal disk, the position of the absorption peak in the LWIR window can be shifted, and the effect of changing the dielectric material on the absorption peak in MWIR is more notable. We hope that our design will help in the development of metamaterial absorbers for application in thermal imaging and infrared spectroscopy.

Acknowledgements

This work was supported by the grants from National Natural Science Foundation of China (NSFC) (61735018, 61376122, and 61805242); Scientific and Technological Development Project of Jilin province (20170204077GX, 20190103014JH); Excellent Member of Youth Innovation Promotion Association CAS (Y201836, 2014193); Leading Talents and Team Project of Scientific and Technological Innovation for Young and Middle-aged Groups in Jilin Province (20190101012JH); Overseas Students Science and Technology Innovation and Entrepreneurship Projects; Project of CIOMP-Duke Collaborative Research (201203002); Project of CIOMP-Fudan University Collaborative Research; Independent fund of State Kay Laboratory of Applied Optics.

Conflict of Interest

The authors declare no conflict of interest.

Keywords

infrared, metamaterial absorbers, plasmon resonance

Received: March 20, 2020
Revised: July 13, 2020
Published online: August 16, 2020

[1] H. Lin, B. C. P. Sturmberg, K. - T. Lin, Y. Yang, X. Zheng, T. K. Chong, C. M. de Sterke, B. Jia, *Nat. Photonics* **2019**, *13*, 270.
[2] Y. Yao, R. Shankar, M. A. Kats, Y. Song, J. Kong, M. Loncar, F. Capasso, *Nano. Lett.* **2014**, *14*, 6526.
[3] J. Huang, C. Liu, Y. Zhu, S. Masala, E. Alarousu, Y. Han, A. Fratalocchi, *Nat. Nanotechnol.* **2016**, *11*, 60.
[4] H. Zhu, F. Yi, E. Cubukcu, *Nat. Photonics* **2016**, *10*, 709.
[5] J. N. Anker, W. P. Hall, O. Lyandres, N. C. Shah, J. Zhao, R. P. Van Duyne, *Nat. Mater.* **2008**, *7*, 442.
[6] C. Li, Q. Wang, *ACS Nano*. **2018**, *12*, 9654.
[7] Y. Gong, Z. Wang, K. Li, L. Uggalla, J. Huang, N. Copner, Y. Zhou, D. Qiao, J. Zhu, *Opt. Lett.* **2017**, *42*, 4537.
[8] T. D. Dao, K. Chen, S. Ishii, A. Ohi, T. Nabatame, M. Kitajima, T. Nagao, *ACS Photonics* **2015**, *2*, 964.
[9] X. Liu, T. Starr, A. F. Starr, W. J. Padilla, *Phys. Rev. Lett.* **2010**, *104*, 207403.
[10] Y. Cui, Y. He, Y. Jin, F. Ding, L. Yang, Y. Ye, S. Zhong, Y. Lin, S. He, *Laser Photonics Rev.* **2014**, *8*, 495.
[11] N. I. Landy, S. Sajuyigbe, J. J. Mock, D. R. Smith, W. J. Padilla, *Phys. Rev. Lett.* **2008**, *100*, 207402.
[12] J. Grant, Y. Ma, S. Saha, A. Khalid, D. R. S. Cumming, *Opt. Lett.* **2011**, *36*, 3476.
[13] L. Lei, S. Li, H. Huang, K. Tao, P. Xu, *Opt. Express* **2018**, *26*, 5686.
[14] W. Guo, Y. Liu, T. Han, *Opt. Express* **2016**, *24*, 20586.
[15] K. Üstün, G. Turhan-Sayan, *J. Appl. Phys.* **2016**, *120*.
[16] W. L. Barnes, A. Dereux, T. W. Ebbesen, *Nature* **2003**, *424*, 824.
[17] J. E. Raynolds, B. A. Munk, J. B. Pryor, R. J. Marhefka, *J. Appl. Phys.* **2003**, *93*, 5346.
[18] D. Ö. Güney, T. Koschny, C. M. Soukoulis, *Phys. Rev. B* **2009**, *80*.
[19] W. Ma, D. Jia, Y. Wen, X. Yu, Y. Feng, Y. Zhao, *Opt. Lett.* **2016**, *41*, 2974.
[20] T. Maier, H. Brueckl, *Opt. Lett.* **2010**, *35*, 3766.
[21] S. Ogawa, M. Kimata, *Materials* **2018**, *11*.
[22] Z. H. Jiang, S. Yun, F. Toor, D. H. Werner, T. S. Mayer, *ACS Nano* **2011**, *5*, 4641.
[23] X. Xiong, Z. H. Xue, C. Meng, S. C. Jiang, Y. H. Hu, R. W. Peng, M. Wang, *Phys. Rev. B* **2013**, *88*, 115105.
[24] X. Xiong, S. C. Jiang, Y. H. Hu, R. W. Peng, M. Wang, *Adv. Mater.* **2013**, *25*, 3994.
[25] S. Bhattacharyya, S. Ghosh, D. Chaurasiya, K. V. Srivastava, *Appl. Phys. A* **2014**, *118*, 207.
[26] D. Wu, C. Liu, Y. Liu, L. Yu, Z. Yu, L. Chen, R. Ma, H. Ye, *Opt. Lett.* **2017**, *42*, 450.
[27] Y. Zhou, Z. Liang, Z. Qin, E. Hou, X. Shi, Y. Zhang, Y. Xiong, Y. Tang, Y. Fan, F. Yang, J. Liang, C. Chen, J. Lai, *Opt. Express* **2020**, *28*, 1279.
[28] X. Liu, T. Tyler, T. Starr, A. F. Starr, N. M. Jokerst, W. J. Padilla, *Phys. Rev. Lett.* **2011**, *107*, 045901.
[29] Z. Zhou, H. Li, J. Cao, H. Tao, in *2017 IEEE 30th International Conference on Micro Electro Mechanical Systems (MEMS)*, IEEE, Piscataway, NJ, USA **2017**, pp. 974.
[30] S. Wang, C. Cai, M. You, F. Liu, M. Wu, S. Li, H. Bao, L. Kang, D. H. Werner, *Opt. Express* **2019**, *27*, 19436.
[31] K. Zhang, M. Wang, S. Yang, *IEEE Trans. Geosci. Remote Sensing* **2017**, *55*, 1363.
[32] J. Grant, I. J. McCrindle, D. R. Cumming, *Opt. Express* **2016**, *24*, 3451.
[33] A. D. Rakić, *Appl. Opt.* **1995**, *34*, 4755.
[34] A. D. Rakić, A. B. Djurišić, J. M. Elazar, M. L. Majewski, *Appl. Opt.* **1998**, *37*, 5271.
[35] D. F. Edwards, E. Ochoa, *Appl. Opt.* **1980**, *19*, 4130.
[36] B. J. Lee, L. P. Wang, Z. M. Zhang, *Opt. Express* **2008**, *16*, 11328.
[37] R. Feng, J. Qiu, L. Liu, W. Ding, L. Chen, *Opt. Express* **2014**, *22*, A1713.
[38] M. Debenham, *Appl. Opt.* **1984**, *23*, 2238.
[39] C. A. Klein, *Appl. Opt.* **1986**, *25*, 1873.
[40] H. Li, *J. Phys. Chem. Ref. Data* **1984**, *13*, 103.

